Polypyrrole nanostructures modified with mono- and bimetallic nanoparticles for photocatalytic H2 generation

Xiaojiao Yuan, Diana Dragoe, Patricia Beaunier, Daniel Bahena Uribe, Laurence Ramos, Maria Guadalupe Méndez-Medrano, Hynd Remita

HAL Id: hal-03437340

https://hal.science/hal-03437340

Submitted on 23 Nov 2021

Polypyrrole Nanostructures Modified with Mono- and Bimetallic Nanoparticles for Photocatalytic H₂ Generation

Xiaojiao Yuan[1], Diana Dragoe[2], Patricia Beaunier[3], Daniel Bahena Uribe[4], Laurence Ramos[5], Maria Guadalupe Méndez-Medrano[6], Hynd Remita[1*]

[1] Laboratoire de Chimie Physique, UMR 8000 CNRS, Université Paris-Sud, Université Paris-Saclay, 91405 Orsay, France

[2] Institut de Chimie Moléculaire et des Matériaux d'Orsay, UMR 8182 CNRS, Université Paris-Sud, Université Paris-Saclay, 91405 Orsay, France

[3] Sorbonne Université, CNRS UMR-7197, LRS, 4 Place Jussieu 75005 Paris, France

[4] Laboratorio Avanzado de Nanoscopía Electrónica, Centro de Investigación y de Estudios Avanzados Del I.P.N, Av. Instituto Politécnico Nacional 2508, San Pedro Zacatenco, C.P, 07360, Ciudad de México, Mexico

[5] Laboratoire Charles Coulomb (L2C), Université de Montpellier, UMR 5221 CNRS, 34095 Montpellier, France

[6] Laboratoire de Physique des Interfaces et des Couches Minces, UMR 7647 CNRS, École Polytechnique, 91120 Palaiseau, France

Abstract

Green hydrogen production by photocatalysis offers a promising way to solve environment and energy issues. Conjugated polymer nanostructures have been demonstrated as a new class of photocatalysts. Here we report that polypyrrole

nanostructures are very promising for hydrogen generation. Lamellar mesophases were used as soft templates to synthesize PPy nanostructures (NSs). The PPy-NSs were modified with mono- and bimetallic (Pt, Ni, Pt-Ni) co-catalyst nanoparticles induced by radiolysis. The modified PPy NSs exhibit excellent photocatalytic activity for H_2 generation and a synergetic effect is obtained with co-modification with Pt and Ni. The effect of the nature of the metal precursors and the loading ratio were studied. We show that the loading rate in co-catalysts is crucial for H_2 generation and an excess of co-catalyst can drastically decrease the activity. The composite photocatalyst PPy-PtNi nanostructures are very active and stable with cycling.

1. Introduction

Hydrogen is a clean, promising and environmental friendly energy source to solve the energy crisis and environmental pollution. The production of hydrogen through a photocatalytic water-splitting process (WSP) has attracted increasing attention.[1-3] Many studies have focused on inorganic metal oxides (e.g., TiO_2,[4, 5] $BiVO_4$,[6] ZnO[7]), (oxy)sulfides (e.g., CdS,[8] SnS_2[9]), and (oxy)nitrides (such as InN,[10] GaN[11]), which are often based on metal cations possessing d^0 and d^{10} electronic configurations, but generally confined by the relatively limited properties such as large band gap, photocorrosion and self-oxidation.[12, 13]

2

Conjugated polymers (CPs) are attracting increasing attention owing to their delocalized conjugated system and outstanding electrochemical property, electrical conductivity, and high carrier mobility. CPs usually have narrow and tunable band gaps, and can absorb UV−Vis and/or near-infrared lights efficiently. We have demonstrated that conjugated polymer nanostructures, such as poly(diphenylbutadyine) (PDPB),[14] poly(3,4-ethylenedioxythiophene) (P3HT),[15] poly(3-hexylthiophene) (PEDOT),[16] and polypyrrole (PPy)[17, 18] exhibit high photocatalytic activities under ultraviolet and visible light irradiation, while their bulk counterpart is not active. We have demonstrated that nanostructuration is a key factor for photocatalytic application of CPs. These conjugated polymer nanostructures were found more active than plasmonic TiO_2 under visible light for water treatment and emerge as a new class of photocatalysts.[17] CPs are also excellent conductive supports for stabilizing co-catalysts to enhance their properties or extend their functions.[19-23]

Incorporation of metals into semiconductors has demonstrated to be a promising way to promote charge carrier separation.[24] Pt-based nanoparticles have attracted a lot of interest for applications in catalysis, fuel cells, and photocatalysis.[25, 26] However, because of high cost and scariness of platinum, its replacement by low cost and abundant catalysts (or co-catalysts) is desirable, but remains a great challenge.[27] Many studies focus on the decrease of the loading with this precious metal by alloying it with another metal of lower cost to increase the photocatalytic activity of the modified photocatalyst for hydrogen evolution. Strategies using Pd-Pt,[28, 29] Ni-Pt[30, 31] or multi-metallic[27] heterojunctions have been investigated. Formation of alloys can reduce the

metal-metal interatomic distance, induce electronic effects, greatly increase the number of active sites and accelerate the mass transfer between the different active sites.[32]

Here we report for the first time that these modified conjugated polymer polypyrrole nanostructures with mono (Pt, Ni) and bimetallic (Pt-Ni) nanoparticles (NPs) are very active for hydrogen generation. Polypyrrole (PPy) nanostructures were synthesized in soft templates formed by lamellar mesophases. Metal nanoparticles (Pt, Ni, and Pt-Ni nanoalloys) of homogeneous size and distribution induced by radiolysis were supported on PPy NPs. Radiolysis is an efficient technique to synthesize metal nanoparticles (NPs) and especially bimetallic NPs of controlled size, distribution and structure in solutions, heterogeneous media or on supports.[33, 34] The obtained composite NSs showed excellent photocatalytic performance for hydrogen generation. The photocatalytic activity of the composite nanomaterials with various metal loading was investigated for hydrogen generation under UV-visible light irradiation.

2. Experimental section

2.1. Chemical reagents. Pyrrole (Py, C_4H_5N, 98%), as monomer, iron chloride ($FeCl_3$) as oxidative agent, sodium dodecyl sulfate (SDS) as surfactant, sodium chloride (NaCl), cyclohexane (C_6H_{12}, 99.7%), and n-pentanol ($C_5H_{12}O$, ≥99%) as co-surfactant were used to synthesize PPy NSs. Platinum(II) acetylacetonate (Pt ($C_5H_7O_2$)$_2$, ≥99.98%) and nickel(II) acetylacetonate ($C_{10}H_{14}NiO_4$, 95%) were used as platinum and nickel precursors, respectively. All the reagents and methanol (CH_3OH, 99.9%) were purchased from Sigma-Aldrich, and ethanol (CH_3CH_3OH, ≥99%) was purchased from

VWR International. Deionized water (Milli-Q, 18.6 MΩ) was used throughout all experiments. All the reagents were pure and used without further purification.

2.2. Materials preparation.

(*i*) **Synthesis of PPy NSs:** The conjugated polymer nanostructures, polypyrrole (PPy NSs), was prepared using the methodology described in previous publications, but with small modifications.[18] Briefly, lamellar mesophases were used as a soft template. These mesophases were formed by SDS (0.8 mg) as surfactant, aqueous solution (2 mL) containing NaCl (0.1 M), Pyrrole (100 μL) in cyclohexane (6 mL) as oil phase, n-pentanol (1.2 mL) as a co-surfactant, and FeCl₃ (64.8 mg) (for monomer oxidation) in water phase. One mesophase containing Py and one mesophase containing FeCl₃ were mixed (as indicated in **Figure 1a-b**). After 5 minutes, the mesophase obtained after mixing turned from transparent to black indicating the oxidation of Py and its polymerization. The PPy-NSs were extracted by simple washing with ethanol and centrifugation. A black powder was obtained after washing with ethanol and drying in the oven at 60 °C.
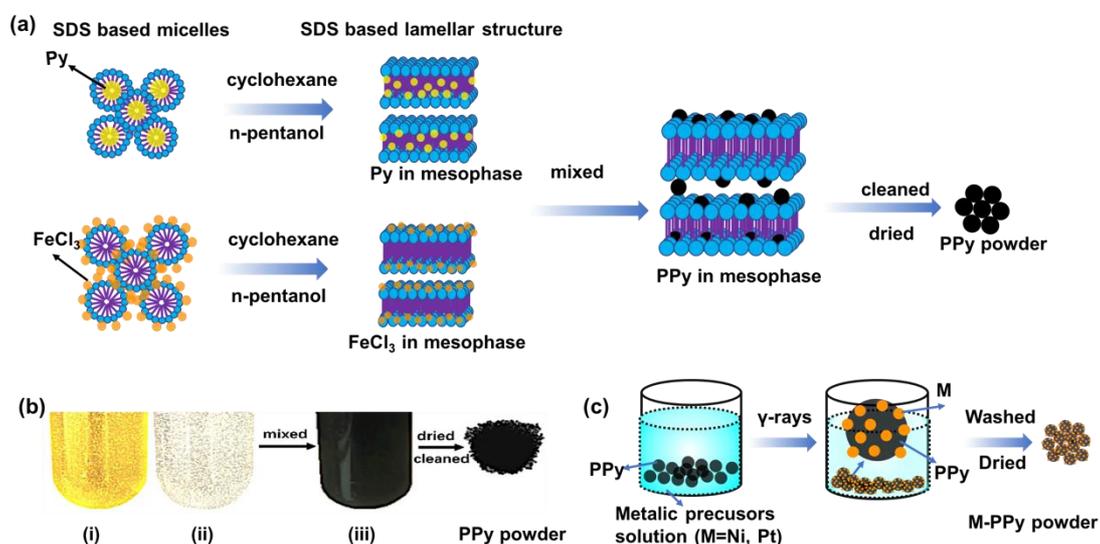
Figure 1. (a) Synthesis process of PPy-NSs using a soft template (a lamellar mesophase); (b) Doped mesophases with (i) FeCl$_3$ and (ii) Py; (iii) PPy-NSs in mesophase; (c) Radiolytic synthesis of metal nanoparticles on PPy NSs (the composite nanomaterials are labeled M-PPy-NSs).

(*ii*) **Pt-PPy-NSs, Ni-PPy-NSs and PtNi-PPy-NSs synthesis:** The metal ions were reduced by solvated electrons and alcohol radicals induced by solvent radiolysis.[35] For each sample, 20 mg PPy-NSs were added into 25 mL of an aqueous solution containing 0.1 M of ethanol (added as HO$^·$ radical scavenger)[33] and the metallic precursors. N$_2$ was bubbled for 15 minutes to remove oxygen. Then, the samples were exposed to ^{60}Co panoramic γ-source at a dose rate of 4 kGy·h^{-1} for 30 minutes (dose 2.0 kGy). After irradiation, the suspensions were centrifuged and washed with water (10 mL) for 3 times. Then, the samples were dried at 50 ℃ for 2 h (**Figure 1c**). Different metal loadings were labeled as x%M-PPy-NSs, where x% indicates the percentage in mass of the metal with respect to the mass of PPy. The materials were collected by centrifugation. The supernatant was completely transparent indicating that all the metallic species were deposited on the PPy nanostructures.

2.3. Characterization

Small Angle X-Ray Scattering (SAXS) was used to characterize the mesophases before and after polymerization. The mesophases doped with only Py, only FeCl$_3$ and containing PPy (obtained after oxidation of Py with FeCl$_3$) were put in glass capillaries (diameter =1.5 mm) and high brightness X-Ray tube with low power and an aspheric multilayer optic (GeniX 3D from Xenocs) were employed to deliver an ultralow

divergent beam (0.5 mrad). A two-dimensional Schneider 2D image plate detector prototype was used to collect the scattered intensity.

Mott-Schottky (MS) plots measurement was carried out by using a typical three electrode setup (Pt wire and Ag/AgCl as counter and reference electrodes, respectively). PPy film on FTO as working electrode. The MS spectra were measured in the voltage window of 0.2 V~1.0 V in the dark (increment: 20 mV, frequency: 1 kHz). An aqueous solution of 1 M $NaSO_4$ was used as electrolyte.

UV-Vis adsorption spectra were recorded with a HP 8453 spectrophotometer.

The size, dispersion and morphology of the conducting polymer nanostructures and metal nanoparticles were examined by scanning electron microscopy (SEM, ZEISS Supra 55 V P FEG-SEM) and transmission electron microscopy (TEM, JEOL JEM 2010 UHR operating at 200 kV). The chemical analyses were obtained by Energy-Dispersive X-ray Spectroscopy (EDS) microanalyzer (PGT-IMIX PC) mounted to the microscope. High Angle Annular Dark Field images were obtained using Scanning Transmission Electron Microscopy Cs corrected JEOL-ARM-200F at 200 kV.

XPS measurements were performed on a K Alpha spectrometer from ThermoFisher, equipped with a monochromated X-ray Source (Al K$_{\alpha}$, 1486.6 eV) with a spot size of 400 µm. The hemispherical analyzer was operated in CAE (Constant Analyser Energy) mode, with a pass energy of 200 eV and a step of 1 eV for the acquisition of surveys spectra, while for the acquisition of narrow scans, a pass energy of 50 eV and 100 eV and a step of 0.1 eV were used. The charge build-up was neutralized by means of a "dual beam" flood gun. The obtained spectra were treated by

means of the Avantage software provided by the manufacturer. A Shirley type background subtraction was used and the peak areas were normalized using the Scofield sensitivity factors. The binding energies were calibrated against the C1s binding energy set a 284.8 eV. The peaks were analyzed using mixed Gaussian-Lorentzian curves (70% of Gaussian character).

Photocatalytic Production of Hydrogen

We used methanol as a hole scavenger. Some works have reported that different sacrificial donors without H (such as N_2S or I^-) could enhance the yield of hydrogen during photocatalytic process.[36] However, their photocatalytic activities are not as efficient as methanol as a hole scavenger.

H_2 production from methanol-water mixture solution was assessed in a closed quartz reactor with N_2 atmosphere under vigorous stirring. For the experiments, 20 mg of the photocatalyst was dispersed in 20 mL of a degassed aqueous solution with 25 vol % of methanol, as holes' scavenger. The samples were irradiated by an Oriel 300 W Xenon lamp with an infrared water filter for 5 h under stirring. Every 1 h, 0.2 mL gas sample was taken by a syringe from the quartz reactor. The amount of H_2 was determined by gas chromatography (GC) using Shimadzu GC-14B.

3. Results and discussions

3.1 Characterization

The mesophases doped with Py, with $FeCl_3$ and the mesophase resulting from the mixing of the two previous ones were characterized by small angle X-ray scattering

(SAXS) (see **Figure 2a**). All the three samples are lamellar phases, characterized by two peaks located at scattering vectors q_0 and $2q_0$; The increase of the scattered intensity at small q is also typical of lamellar phases. The spacing (periodicity of the lamellar phase) $d = 2\pi/q_0 = 6.3$ nm is the same for the three samples. We note that the lamellar phase containing the monomer is more ordered (second order peak sharper) than the other samples.

The electrochemical Mott-Schottky measurement was performed to obtain flat band potential which can be given by the intercepts of the extrapolated lines (Slope) (**Figure 2b**). The carrier concentration (N_A) is determined by the equation[37]: $N_A = \frac{2}{e\varepsilon_r\varepsilon_0 Slope}$, e is electron charge, ε_r is the dilecectric constant (~ 10 for PPy), ε_0 is the free space (8.85×10^{-14} Fcm^{-1}). The N_A of PtNi-PPy (17.7×10^{19} m^{-3}) is five times than PPy ($3.5_x 10^{19}$ m^{-3}), indicating enhanced electronic conductivity, which will lead to decrease of charge carrier recombination and better electron transfer.[38, 39]

UV-Vis spectrum of PPy exhibits an absorption in the visible region (400 nm~700 nm) and near-IR region (700 nm ~1000 nm) (**Figure 2c**). The peak at 470 nm is owing to the π-π^* transitions. The corresponding band gap (E_g) of PPy was determined from the Kubelka-Munk function (**Figure 2d**): the value of Eg of PPy was found to be 2.2 eV, which is similar to that of previous reports.[18]
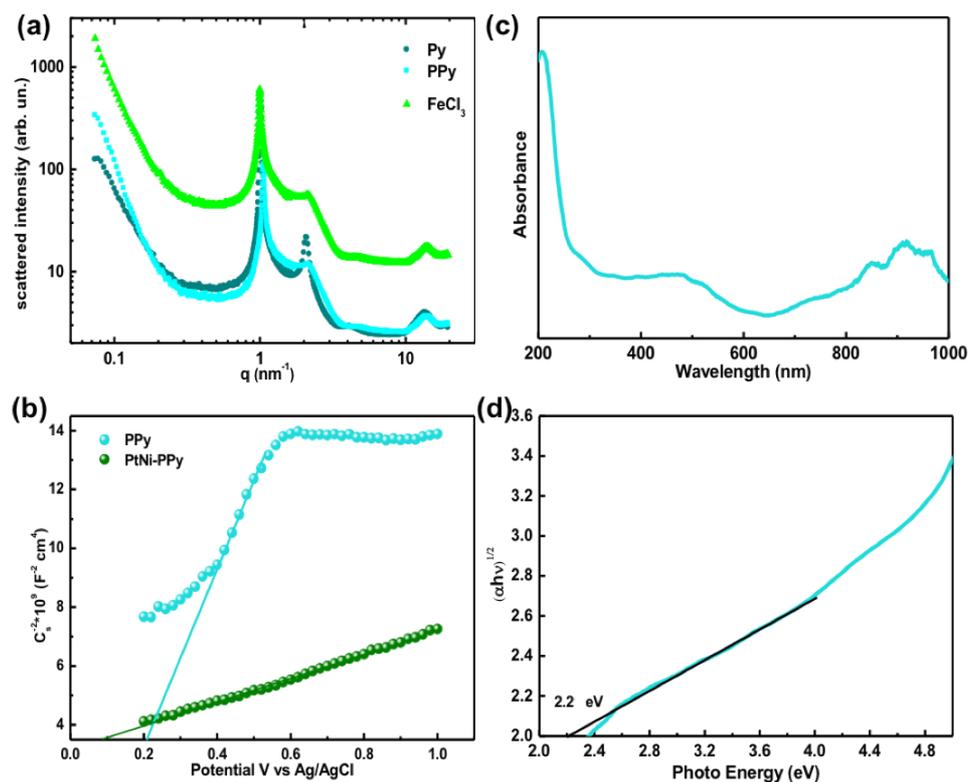
Figure 2. (a) SAXS of the mesophases doped with Py, $FeCl_3$ and the mesophase resulting from the mixing of the two other mesophases and containing PPy (induced by oxidation of Py by Fe^{3+}); (b) Mott-Schottky plot of PPy and PtNi-PPy; (c) UV-Vis spectrum of PPy and (d) corresponding Kubelka-Munk plot.

SEM images show uniform PPy NSs with average size of 40 nm (**Figure S1**). TEM was used to characterize the morphology, size, and distribution of the metal nanoparticles (NPs) synthesized by radiolysis and the composite nanomaterials (**Figure 3).** Aggregates of PPy nanoplates were observed (see **Figure 3 a, c, e**). For platinum modified polymer nanostructures, well dispersed Pt NPs with a diameter of about 2-3 nm were observed on the surface of PPy NSs (**Figure 3a**). **Figure 3b** shows (111) facets of Pt with interplanar spacing of 0.23 nm indicating the formation of crystalline Pt NPs. For nickel-modified polymer nanostructures, Ni-based NPs of 5-nm diameter and homogeneously dispersed on the surface of PPy-NSs were observed as shown in **Figure**

3c-d. **Figure 3d** presents the interplanar spacing of the Ni-based nanoparticles. The lattice spacings of 0.20 and 0.24 nm correspond to the (111) plane of Ni and the (111) plane of NiO, respectively, which proves the presence of Ni^0-NiO-based nanoparticles on PPy NSs. In case of co-modification with Pt and Ni, metal NPs of homogeneous size (2 nm) were observed in **Figure 3e** showing a smaller crystallite size than monometallic NPs, which support the formation of Pt-Ni nanoalloys.[40] High-resolution STEM images (**Figure 3f**) present the lattice spacing of 0.22 nm and 0.19 nm, which are indexed as the (111) and (200) planes of the fcc PtNi alloys, respectively. EDS analysis of the metal nanoparticles shows that the nanoparticles contain both Pt and Ni **(Figure S2)** indicating the bimetallic nature of the NPs.

The surface composition and the oxidation states of the metal NPs in the modified PPy NSs were analyzed by X-ray photospectroscopy (XPS). XPS patterns of Pt-PPy-NSs, Ni-PPy-NSs and PtNi-PPy-NSs are shown in **Figure 4**.
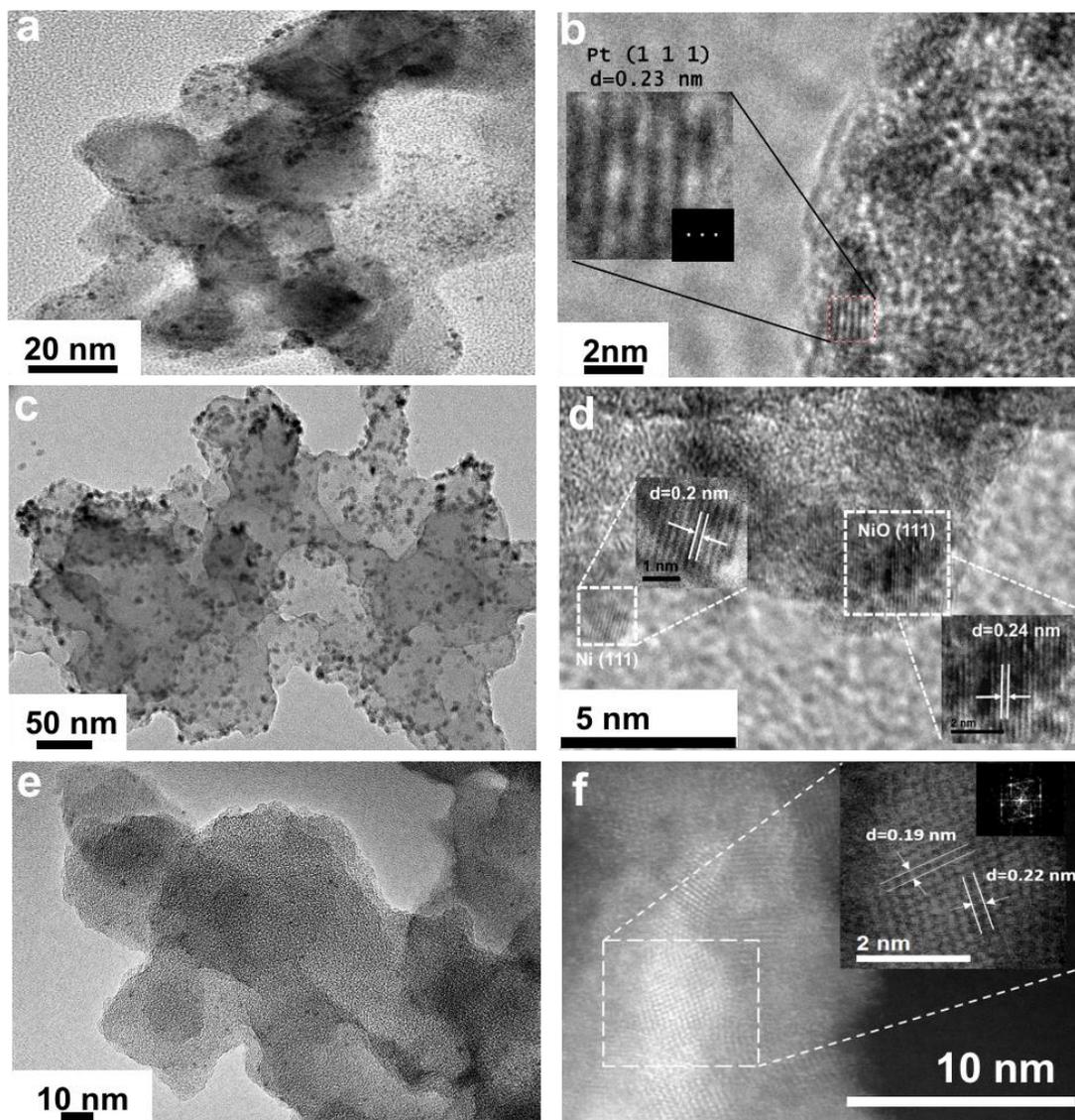
Figure 3. TEM images of 0.2%Pt-PPy-NSs (a-b), 5%Ni-PPy-NSs (c-d), 0.05%Pt0.05%Ni-PPy-NSs (e) and HAADF-STEM image of 0.05%Pt0.05%Ni-PPy (f).

Wide region of spectroscopy of PtNi-PPy-NSs is shown in **Figure S3.** The signals at 284.1 eV, 402.5 eV, 533.2 eV and 201.2 eV correspond to C 1s, N 1s, O 1s and Cl 2p, respectively, which are due to PPy.[32, 41] Other signals at 70.5 eV and 53.3 eV correspond to Pt 4f and Ni 3p respectively. The narrow range spectra of C 1s and N 1s are depicted in **Figure 4a-b**, which also proves the presence of PPy.

The Pt 4f core-level spectrum shows an intense doublet at 71.7 eV and 75.0 eV corresponding to Pt $4f_{7/2}$ and Pt $4f_{5/2}$ of Pt^0 which indicates that Pt^{2+} was reduced into Pt metal in Pt-PPy-NSs sample (**Figure 4c**).

The Ni2p core-level spectrum shows the presence of metallic nickel, the component $Ni2p_{3/2}$ at 852.5 eV, alongside with its oxide, and hydroxide, which are expected as nickel is very sensitive to oxygen (**Figure 4d**).[42-44]

Given the low loading levels of both Ni and Pt, especially in the case of PtNi-PPy-NSs (**Figure 4e-f**), the acquisition conditions were adjusted in order to have the best possible signal/noise ratio in detriment of spectral resolution. **Figure 4e-f** shows that Pt and Ni nanoparticles are partly oxidized. The Pt 4f signals represent an intense doublet at 71.4 eV and 74.7 eV, corresponding to the core level energies of Pt $4f_{2/7}$ and Pt $4f_{5/2}$ of Pt metal. Other doublets (71.4 eV and 75.9 eV) and (75.0 eV and 77.9 eV) can be ascribed to the +2 and +4 oxidations of Pt, respectively. The peaks at 68.0 eV and 72.4 eV correspond to the Ni $3p_{3/2}$ and Ni $3p_{1/2}$ correspond to NiO (**Figure 4e**).[32, 45] **Figure 4f** shows the presence of Ni metal, NiO and $Ni(OH)_2$. The presence of the oxidized Pt and Ni species is probably caused by the air during the XPS analysis. It is noteworthy that, in the bimetallic materials (PtNi), the banding energy of Pt is slightly lower by 0.3 eV compared to the monometallic Pt-PPy, which indicates the strong interaction between the metals and PPy supports.[46]
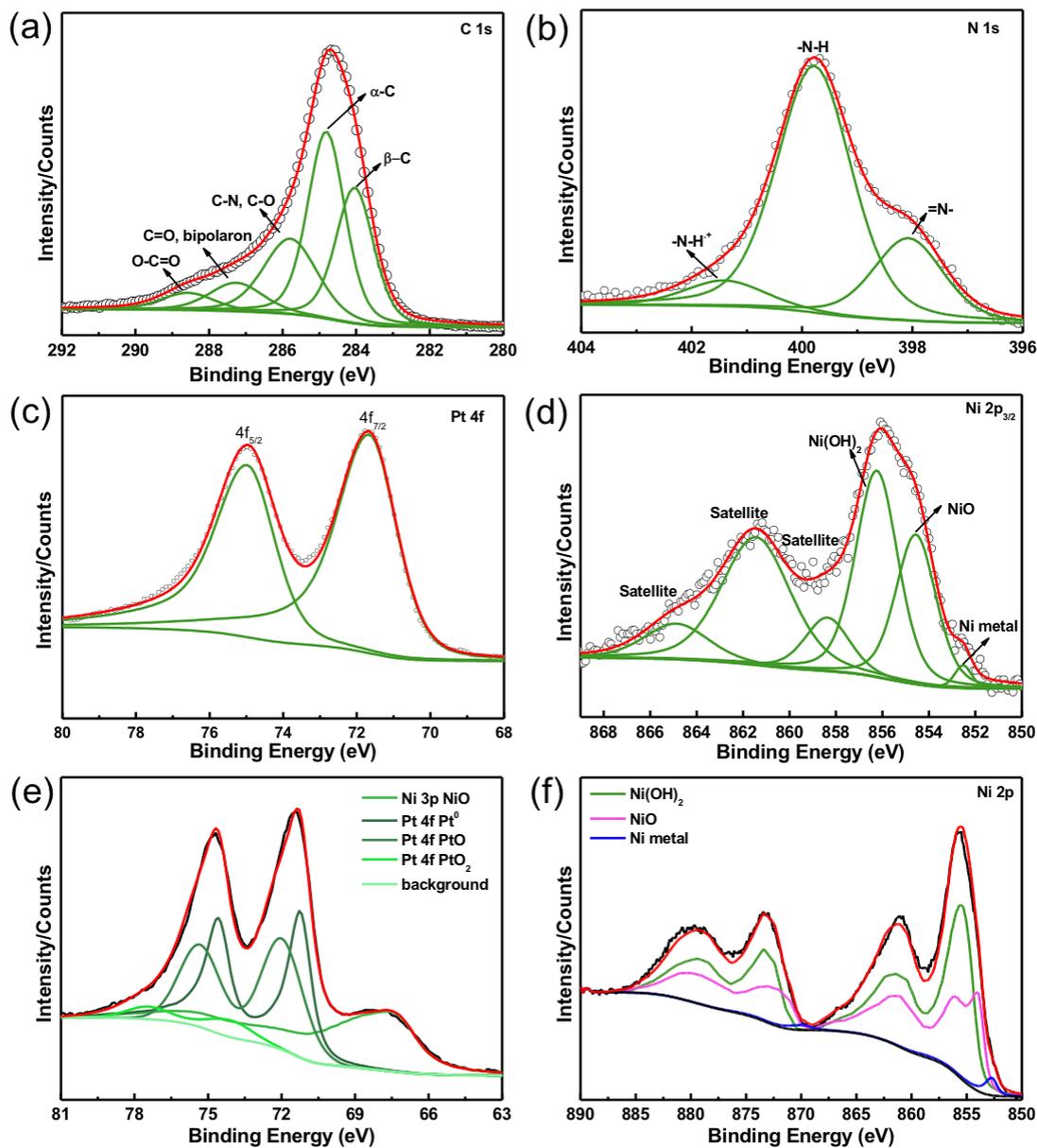
Figure 4. XPS spectra of (a) C1s, (b) N1s in PtNi-PPy-NSs, (c) Pt 4f in Pt-PPy-NSs, (d) narrow scan spectrum of Ni 2p in Ni-PPy-NSs, (e) narrow scan spectrum of nickel states in PtNi-PPy-NSs and (f) narrow scan spectrum of Ni 2p in PtNi-PPy-NSs.
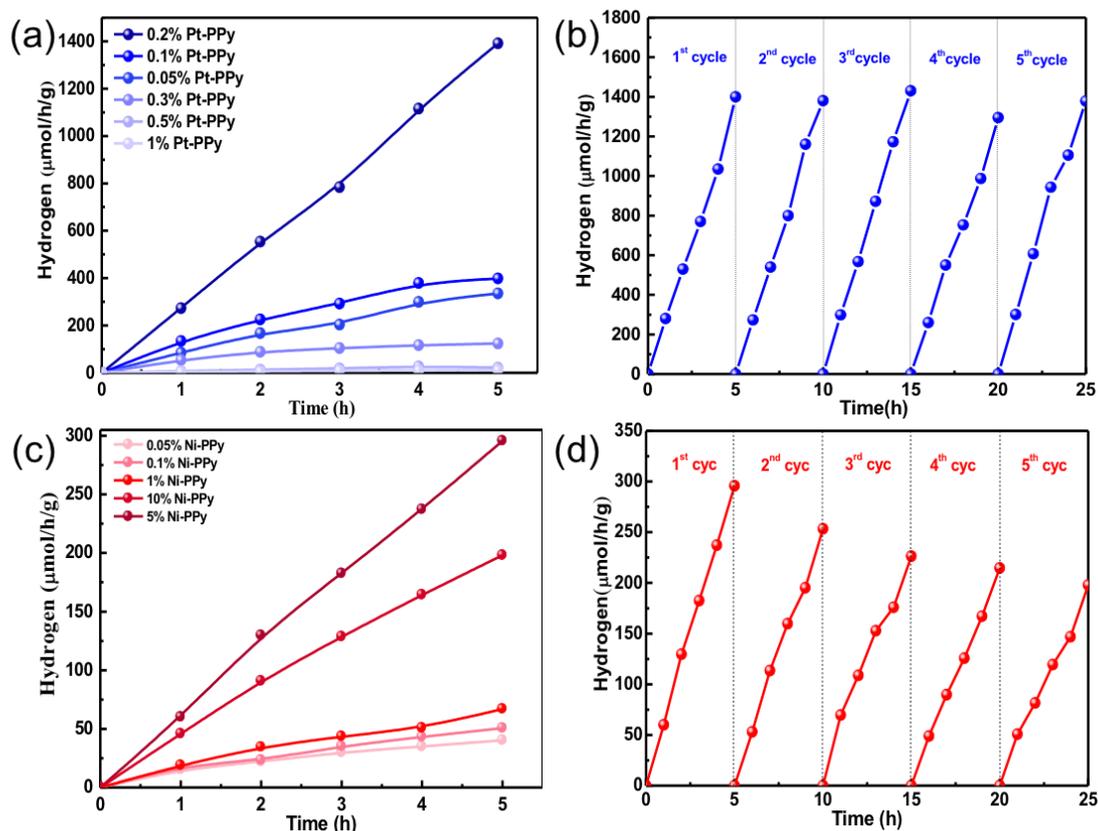
3.2 Photocatalytic H_2 generation

The addition of co-catalyst (such as Pt, Ni-NiO, PtNi) NPs for photocatalytic hydrogen generation can reduce the activation energy of the reaction, provide an active site for proton reduction and H-H bond formation and decrease the recombination of

charge carriers, resulting in an improvement of photocatalytic activity for hydrogen production.[43, 44] In addition, the amount of loading of the co-catalyst is also a crucial factor for hydrogen generation.[47]

Pt-PPy-NSs

Noble metals with a low Fermi level can trap electrons from the conduction band (CB) of the semiconductor. Among these noble metals, Pt is the best candidate as co-catalyst for hydrogen production due to its largest work function.[48] The photocatalytic H_2 generation efficiency of as-prepared samples was investigated in 25 vol.% methanol aqueous solution under UV-vis light. As shown in **Figures 5a**, with time increase, 0.2%Pt-PPy-NSs show a remarkable enhancement in the photocatalytic activity. Interestingly 0.05%Pt-PPy-NSs and 0.1%Pt-PPy-NSs present higher photocatalytic performance compared with nanostructures comprising higher loadings in Pt (0.3%, 0.5% and 1% loading rate). This indicates that higher photocatalytic activity is obtained with a very small amount of co-catalyst. The H_2 production rate with 0.2%Pt-PPy-NSs is 1400 μmol/h/g, and the H_2 production rates with 0.05%Pt-PPy-NSs and 0.1%Pt-PPy-NSs are 312 and 341 μmol/h/g, respectively. For loading larger than 0.2%, the H_2 production rate decreases dramatically, showing that an excess metal loading can induce a dramatic decrease of the photocatalytic activity. At high loading, metal nanoparticles can play the role of recombination centers, inducing a decrease in the photocatalytic activity.[49] Higher metal loading can also induce hindering of the absorption of light by the semiconductor.

The stability of the photocatalytic activity was investigated with 0.2%Pt-PPy-NSs under UV-visible light (see **Figure 5b**). Modified PPy nanostructures with Pt NPs show a very good stability with cycling.

Figure 5. (a) A comparison of the photocatalytic H_2 generation rate for different loading rates of PPy-NSs in Pt as indicated in the legend; (b) Hydrogen production with 0.2%Pt-PPy-NSs after 4 cycles of 5 h; (c) A comparison of the photocatalytic H_2 generation rate for different loading rates of Ni on PPy-NSs as indicated in the legend; (d) Hydrogen production with cycling in the presence of 5%Ni-PPy-NSs.

Ni-PPy-NSs

Ni is also a very promising candidate as co-catalyst for H_2 production owing to its low-cost and high photocatalytic properties.[43, 44, 50] Ni nanoparticles do not only provide

a large surface area and active sites, but also decrease the electron-hole recombination.[43, 44] As shown in **Figure 5c**, the photocatalytic activity of Ni-PPy-NSs increases with the Ni loading until 5% loading, then a decrease in the photocatalytic activity is observed. Interestingly, 5%Ni-PPy-NS exhibits excellent photocatalytic activity for hydrogen production (289 μmol/h/g), despite the fact that this rate is much lower than that obtained with 0.2%Pt-PPy-NSs (1400 μmol/h/g). XPS signals show the concomitant presence of NiO and Ni(OH)$_2$ (**Figure 4b**). The Fermi level of NiO is lower than that of Ni^0, therefore, the photogenerated electrons in NiO/Ni structure migrate from the conduction band of the semiconductor to the Ni layer, and then transfer to the NiO layer, which leads to efficient charge carrier separation. Ni(OH)$_2$ as co-catalyst can also efficiently transport photogenerated electrons from the conduction band of the semiconductor to Ni(OH)$_2$/Ni clusters leading to high photocatalytic activity for hydrogen generation.[51]

It is worth mentioning that the nature of the metal precursors is one of the factors that may strongly affect the size, shape and/or the surface state of the metal nanoparticles, and therefore their activity as co-catalysts. Our results show that PPy-NSs modified with metal nanoparticles prepared with platinum (II) acetylacetonate (Pt(C$_5$H$_7$O$_2$)$_2$) and nickel (II) acetylacetonate (Ni(C$_5$H$_7$O$_2$)$_2$), as metallic precursors exhibit higher photocatalytic properties compared with PPy-NSs modified prepared with potassium tetrachloroplatinate (II) (K$_2$PtCl$_4$) and nickel formate (C$_2$H$_2$NiO$_4$), respectively (**Table S1**). Cui and co-workers investigated the influence of the metal precursor ligands on the selectivity of alloy particle shape and structures.[52] Therefore,

the choice of the metal precursor is very important for the co-catalyst activity for hydrogen production.

The stability of Ni-PPy-NSs with cycling was investigated. As shown in **Figure 5d**, after 5 cycles, the amount of H_2 has dropped by 33%. The small decrease of the photoactivity can be due to the leaching of Ni nanoparticles during the photocatalytic cycles. Indeed, Ni is a very efficient catalyst for many reactions, but it is known to leach in water.[53]

PtNi-PPy-NSs

A strategy to avoid Ni leaching with cycling, is to alloy Ni with another noble metal such as Au or Pt. Ni from a Pt-Ni alloy does not dissolve in an electrolyte owing to the $Ni(OH)_2$ passivated surface and the enhanced stability of Ni in the Pt lattice.[45, 54] To investigate the photocatalytic hydrogen production and stability of the bimetallic (PtNi) doping of PPy-NSs, the experiments were conducted with the same total metal loading rate (0.1%) under the same conditions (see in **Figure 6a-c**). Interestingly, we found that a 50/50 mixture of Ni and Pt shows an enhanced photocatalytic activity (664 μmol/h/g) compared with a pure Pt loading (341 μmol/h/g) and a pure Ni loading (52 μmol/h/g) (**Figure 6a** and **Figure S4**). Some related works for photocatalytic H_2 generation with different photocatalysts have been listed in **Table S2** for comparison. The enhanced photocatalytic activity of PtNi-PPy-NSs may be owing to the increased photoefficiency by Schottky barrier leading to longer lifetime of charge carriers and strong UV-vis absorption due to the plasmon resonance of Pt in the UV range.[55] Synergetic effects are

expected (such as electronic and geometry effects) inducing enhancement of photocatalytic activity. Such synergetic effect for hydrogen production with bimetallic nanoparticles was also recently observed for Ni−Au/TiO$_2$ and Ni−Pd/TiO$_2$: The association of Ni with another metal (such as Pd or Au) induces an increase of the photocatalytic activity of semiconductors for hydrogen production.[43, 44, 56] In case of Ni-Pd/TiO$_2$, the study of light absorption, charge-carrier dynamics, and photocatalytic activity revealed that the main role of the metal NPs is to act as catalytic sites for recombination of atomic hydrogen. Platinum is very efficient in electron scavenging and proton reduction, while Ni is a very good co-catalyst for H-H bond formation.[31, 43, 44, 47]

Figure 6b and **Figure S5** show the effect of the total metal loading on photocatalytic hydrogen production for sample with a fixed Pt: Ni ration of 1:1 and the catalytic activity strongly depends on the Ni/Pt ratio (**Figure S6**). The 0.1%PtNi-PPy-NSs exhibits the highest photocatalytic activity yield rate of hydrogen compared with the PPy modified with other loading rates. **Figure 6c** shows very high stability with cycling, which indicates that PtNi-PPy-NSs are much more stable than Ni-PPy-NSs during the photocatalytic cycle tests.
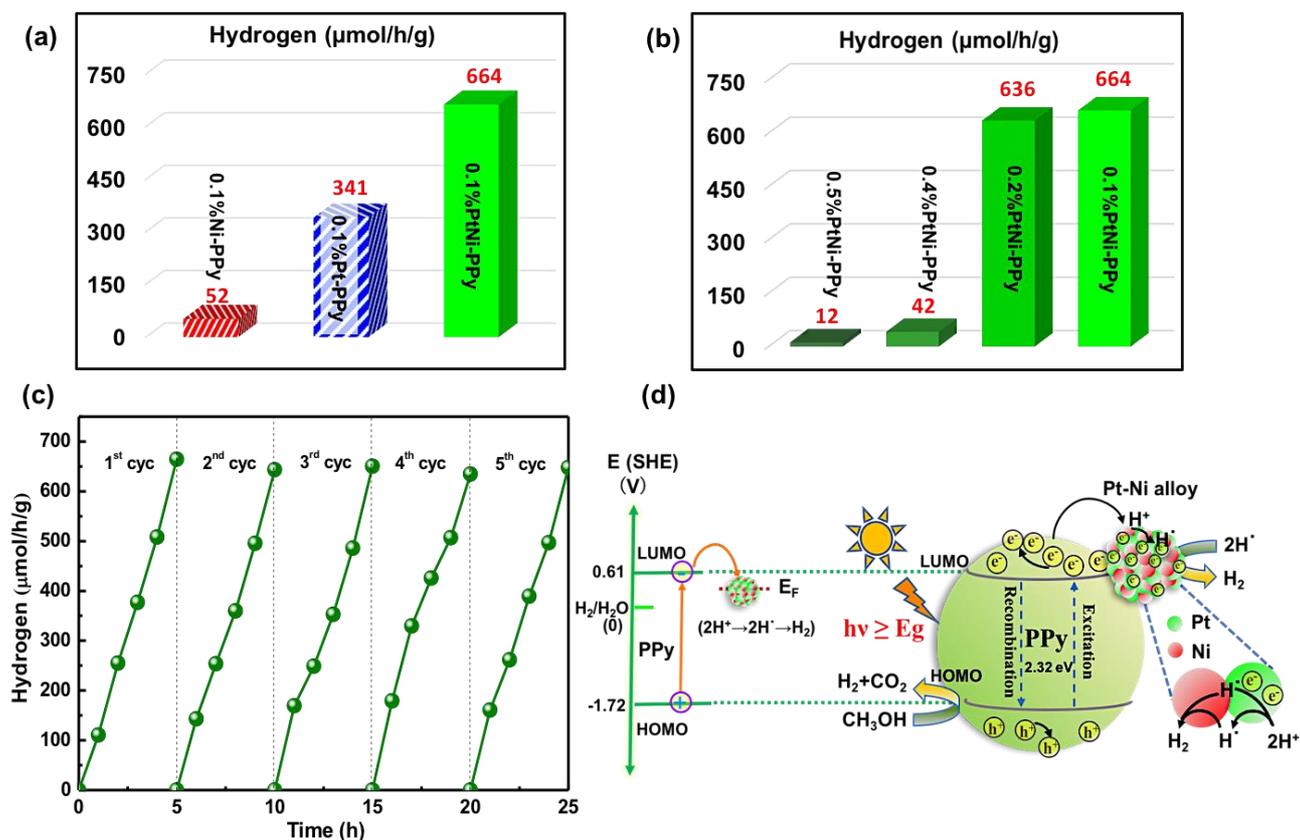
Figure 6 (a) Photocatalytic H_2 generation rate with the same loading rate for different samples. **(b)** The photocatalytic H_2 generation rate for different loading rate of Ni-Pt on PPy-NSs. **(c)** Hydrogen production with cycling in the presence of 0.1%PtNi-PPy-NSs. **(d)** Proposed photocatalytic mechanism for hydrogen generation. Metal NPs act as electron traps, and protons reduction catalysts.

The mechanism of hydrogen formation is similar to that proposed for Pd-Ni/TiO$_2$ and Au-Ni/TiO$_2$.[43, 44] The proposed photocatalytic mechanism for hydrogen generation is shown in **Figure 6d**. The generation of the electron–hole pair takes place in the organic semiconductor PPy NSs. When the energy of the incident light is higher or equal to the band gap of PPy-NSs, the photogenerated electrons can be promoted from the HOMO to the LUMO of PPy nanostructures, leaving holes in the HOMO of PPy-NSs (PPy-NSs → h$^+$+e$^-$). Water molecules are reduced by the electrons to produce H$_2$

($H_2O + e^- \rightarrow H_2 + OH^-$) in the presence of co-catalysts. Methanol was used as a hole scavenger: CH_3OH reacts with the holes to give CO_2 and H_2. This hole scavenging results in better charge carrier separation and leads to enhancement of light conversion quantum yield.[57] Platinum is known to be an efficient sink for electrons.[58] The presence of Pt-based nanoparticles decreases the charge carrier recombination, and therefore induces the increase of the quantum yield. The excited electrons migrate from PPy-NSs to the metal NPs, and then H^+ are reduced on the metal surface to promote the proton reduction to generate atomic hydrogen, while these atomic hydrogen recombine to produce the molecular hydrogen (**Figure 6d**).[59] The metal nanoparticles (such as Pt, Ni and Pt-Ni) not only serve as an electron sinks, but also provide effective proton reduction sites due to its relatively low over-potential.[43] Ni-based nanoparticles are very active co-catalysts in $H^\cdot$ recombination to form H_2.[43, 44] Finally, $H^\cdot$ recombination appears on the surface of the metal NPs producing molecular hydrogen H_2, which is facilitated by the presence of Ni. The enhancement of hydrogen generation compared with that of the monometallic samples is owing to a synergetic effect between Ni and Pt: The presence of Pt induces better electron scavenging and higher $H^\cdot$ production, while the association with Ni promotes $H^\cdot$ recombination leading to higher H_2 production. Furthermore, the modification with bimetallic Pt-Ni nanoparticles leads to photocatalysts with high stability with cycling.

Conclusion

Our study shows that conjugated polymer nanostructures modified with metal nanoparticles are promising for green hydrogen production. PPy nanostructures were successfully synthesized in soft templates formed by lamellar mesophases. Monometallic Pt, Ni-NiO and bimetallic Pt-Ni nanoparticles of homogeneous size and dispersion on the surface of PPy NSs were deposited on PPy-NSs by radiolytic reduction. The modified PPy-NSs are very active in hydrogen generation under UV-visible light, and their photocatalytic activity is very sensitive to the metal loading. 0.2%Pt-PPy-NSs presents the best activity compared with the other percentage loading rates. Modification with nickel-based nanoparticles gives also promising results for green hydrogen production. 5%Ni-PPy-NSs show enhanced photocatalytic performance due to the formation of the heterojunction between PPy and NiO-Ni nanoparticles. However, the phototocatalytic activity decreases slightly with time, probably because of Ni leaching. The choice of the metal precursors used in the NPs synthesis is important for the activity of the metal co-catalysts: The best activities were obtained using Ni and Pt acetylacetonates as precursors for the metal-based nanoparticles. The stability and the photocatalytic activity of Ni-based photocatalysts were much improved by alloying Ni with Pt. Pt-Ni-PPy exhibit higher activity compared to its monometallic counterparts, and a synergetic effect is obtained. The presence of Pt leads to better electron scavenging and higher $H^{.}$ formation, while the association with Ni promotes $H^{.}$ recombination leading to higher H_2 generation. These nanostructures are also very stable with cycling.

Further studies will focus on development of composite materials based on conjugated polymer nanostructures modified with co-catalysts made of abundant elements for solar fuel production.

Reference

1.   A. Kudo and Y. Miseki, *Chemical Society Reviews*, 2009, **38**, 253-278.

2.   T. Hisatomi, J. Kubota and K. Domen, *Chemical Society Reviews*, 2014, **43**, 7520-7535.

3.   K. Maeda, A. Xiong, T. Yoshinaga, T. Ikeda, N. Sakamoto, T. Hisatomi, M. Takashima, D. Lu, M. Kanehara and T. Setoyama, *Angewandte Chemie*, 2010, **122**, 4190-4193.

4.   J. Yu, L. Qi and M. Jaroniec, *The Journal of Physical Chemistry C*, 2010, **114**, 13118-13125.

5.   A. Tanaka, S. Sakaguchi, K. Hashimoto and H. Kominami, *ACS Catalysis*, 2012, **3**, 79-85.

6.   P. Li, X. Chen, H. He, X. Zhou, Y. Zhou and Z. Zou, *Advanced Materials*, 2018, **30**, 1703119.

7.   B. E. Sernelius, K.-F. Berggren, Z.-C. Jin, I. Hamberg and C. G. Granqvist, *Physical Review B*, 1988, **37**, 10244.

8.   S. Chen and L.-W. Wang, *Chemistry of Materials*, 2012, **24**, 3659-3666.

9.   T. Di, B. Zhu, B. Cheng, J. Yu and J. Xu, *Journal of Catalysis*, 2017, **352**, 532-541.

10.   Z. Su, H. Li, P. Chen, S. Hu and Y. Yan, *Catalysis Science & Technology*, 2017, **7**, 5105-5112.

11.	M. G. Kibria, R. Qiao, W. Yang, I. Boukahil, X. Kong, F. A. Chowdhury, M. L. Trudeau, W. Ji, H. Guo and F. Himpsel, *Advanced Materials*, 2016, **28**, 8388-8397.

12.	G. Liao, Y. Gong, L. Zhang, H. Gao, G.-J. Yang and B. Fang, *Energy & Environmental Science*, 2019.

13.	Y. Inoue, *Energy & Environmental Science*, 2009, **2**, 364-386.

14.	S. Ghosh, N. A. K, L. Ramos, S. Remita, A. Dazzi, A. Deniset-Besseau, P. Beaunier, F. Goubard, P.-H. Aubert & H. Remita, *Nature Materials*, 2015, **14**, 505-511.

15.	D. Floresyona, F. Goubard, P.-H. Aubert, I. Lampre, J. Mathurin, A. Dazzi, S. Ghosh, P. Beaunier, F. Brisset, S. Remita, L. Ramos and R. Hynd, *Applied Catalysis B: Environmental*, 2017, **209**, 23-32.

16.	S. Ghosh, N. A. Kouame, S. Remita, L. Ramos, F. Goubard, P.-H. Aubert, A. Dazzi, A. Deniset-Besseau and H. Remita, *Scientific Reports*, 2015, **5**, 18002.

17.	S. Ghosh, T. Maiyalagan and R. N. Basu, *Nanoscale*, 2016, **8**, 6921-6947.

18.	X. Yuan, D. Floresyona, P.-H. Aubert, T.-T. Bui, S. Remita, S. Ghosh, F. Brisset, F. Goubard and H. Remita, *Applied Catalysis B: Environmental*, 2019, **242**, 284-292.

19.	T. K. Das and S. Prusty, *Polymer-plastics Technology and Engineering*, 2012, **51**, 1487-1500.

20.	S. Günes, H. Neugebauer and N. S. Sariciftci, *Chemical Reviews*, 2007, **107**, 1324-1338.

21.	J. H. Burroughes, D. D. Bradley, A. Brown, R. Marks, K. Mackay, R. H. Friend, P. Burns and A. Holmes, *Nature*, 1990, **347**, 539.

22.	C. X. Guo, M. Wang, T. Chen, X. W. Lou and C. M. Li, *Advanced Energy Materials*, 2011, **1**, 736-741.

23.	G. Zhang, Z. A. Lan and X. Wang, *Angewandte Chemie International Edition*, 2016, **55**, 15712-15727.

24.	N. Bhandary, A. P. Singh, S. Kumar, P. P. Ingole, G. S. Thakur, A. K. Ganguli and S. Basu, *ChemSusChem*, 2016, **9**, 2816-2823.

25.	J. B. Schlenoff and H. Xu, *Journal of the Electrochemical Society*, 1992, **139**, 2397-2401.

26. Y. Holade, A. Lehoux, H. Remita, K. B. Kokoh and T. k. W. Napporn, *The Journal of Physical Chemistry C*, 2015, **119**, 27529-27539.

27. Z. Cai, Z. Lu, Y. Bi, Y. Li, Y. Kuang and X. Sun, *Chemical Communications*, 2016, **52**, 3903-3906.

28. H. Kobayashi, M. Yamauchi, H. Kitagawa, Y. Kubota, K. Kato and M. Takata, *Journal of the American Chemical Society*, 2010, **132**, 5576-5577.

29. Y. Zhao, F. Pan, H. Li, G. Q. Xu and W. Chen, *ChemCatChem*, 2014, **6**, 454-458.

30. N. Cao, J. Su, W. Luo and G. Cheng, *International Journal of Hydrogen Energy*, 2014, **39**, 9726-9734.

31. L. Mao, Q. Ba, S. Liu, X. Jia, H. Liu, W. Chen and X. Li, *RSC Advances*, 2018, **8**, 31529-31537.

32. S. Ghosh, S. Bera, S. Bysakh and R. N. Basu, *ACS Applied Materials & Interfaces*, 2017, **9**, 33775-33790.

33. J. Belloni, M. Mostafavi, H. Remita, J.-L. Marignier and M.-O. Delcourt, *New Journal of Chemistry*, 1998, **22**, 1239-1255.

34. H. Remita and S. Remita, in *Recent Trends in Radiation Chemistry*, World Scientific, 2010, pp. 347-383.

35. H. Remita, M. G. Méndez Medrano and C. Colbeau-Justin, *Visible Light-Active Photocatalysis: Nanostructured Catalyst Design, Mechanisms, and Applications*, 2018, 129-164.

36. A. Galińska and J. Walendziewski, *Energy & Fuels*, 2005, **19**, 1143-1147.

37. S. Tokgöz, Y. Firat, Z. Safi and A. Peksoz, *Journal of The Electrochemical Society*, 2019, **166**, G54-G60.

38. S. Wang, P. Chen, J. H. Yun, Y. Hu and L. Wang, *Angewandte Chemie International Edition*, 2017, **56**, 8500-8504.

39. J. Li, X. Gao, Z. Li, J. H. Wang, L. Zhu, C. Yin, Y. Wang, X. B. Li, Z. Liu and J. Zhang, *Advanced Functional Materials*, 2019, **29**, 1808079.

40. M. Blosi, S. Ortelli, A. Costa, M. Dondi, A. Lolli, S. Andreoli, P. Benito and S. Albonetti, *Materials*, 2016, **9**, 550.

41. M. Šetka, R. Calavia, L. Vojkůvka, E. Llobet, J. Drbohlavová and S. Vallejos, *Scientific Reports*, 2019, **9**, 8465.

42.   Q. Lu, R. Huang, L. Wang, Z. Wu, C. Li, Q. Luo, S. Zuo, J. Li, D. Peng and G. Han, *Journal of Magnetism and Magnetic Materials*, 2015, **394**, 253-259.

43.   A. L. Luna, D. Dragoe, K. Wang, P. Beaunier, E. Kowalska, B. Ohtani, D. Bahena Uribe, M. A. Valenzuela, H. Remita and C. Colbeau-Justin, *The Journal of Physical Chemistry C*, 2017, **121**, 14302-14311.

44.   A. L. Luna, E. Novoseltceva, E. Louarn, P. Beaunier, E. Kowalska, B. Ohtani, M. A. Valenzuela, H. Remita and C. Colbeau-Justin, *Applied Catalysis B: Environmental*, 2016, **191**, 18-28.

45.   K.-W. Park, J.-H. Choi, B.-K. Kwon, S.-A. Lee, Y.-E. Sung, H.-Y. Ha, S.-A. Hong, H. Kim and A. Wieckowski, *The Journal of Physical Chemistry B*, 2002, **106**, 1869-1877.

46.   F. Wang, Y. Jiang, D. J. Lawes, G. E. Ball, C. Zhou, Z. Liu and R. Amal, *ACS Catalysis*, 2015, **5**, 3924-3931.

47.   B. Mei, K. Han and G. Mul, *ACS Catalysis*, 2018, **8**, 9154-9164.

48.   L. Zhang, N. Pan and S. Lin, *International Journal of Hydrogen Energy*, 2014, **39**, 13474-13480.

49.   M. Méndez-Medrano, E. Kowalska, A. Lehoux, A. Herissan, B. Ohtani, S. Rau, C. Colbeau-Justin, J. Rodríguez-López and H. Remita, *The Journal of Physical Chemistry C*, 2016, **120**, 25010-25022.

50.   L. F. Garay-Rodríguez, S. Murcia-López, T. Andreu, E. Moctezuma, L. M. Torres-Martínez and J. R. Morante, *Catalysts*, 2019, **9**, 285.

51.   Y. Xu and R. Xu, *Applied Surface Science*, 2015, **351**, 779-793.

52.   C. Cui, L. Gan, H.-H. Li, S.-H. Yu, M. Heggen and P. Strasser, *Nano letters*, 2012, **12**, 5885-5889.

53.   E. Y. Kaniukov, A. Shumskaya, M. Kutuzau, V. Bundyukova, D. Yakimchuk, D. Borgekov, M. Ibragimova, I. Korolkov, S. Giniyatova and A. Kozlovskiy, *Materials Chemistry and Physics*, 2019, **223**, 88-97.

54.   T. Deivaraj, W. Chen and J. Y. Lee, *Journal of Materials Chemistry*, 2003, **13**, 2555-2560.

55.   S. Shuang, R. Lv, Z. Xie and Z. Zhang, *Scientific Reports*, 2016, **6**, 26670.

56.   S. Oros-Ruiz, R. Zanella, S. E. Collins, A. Hernández-Gordillo and R. Gómez, *Catalysis Communications*, 2014, **47**, 1-6.

57.   P. V. Kamat and S. Jin, *ACS Energy Lett.* 2018, 3, 622-623.

58. E. Kowalska, H. Remita, C. Colbeau-Justin, J. Hupka and J. Belloni, *The Journal of Physical Chemistry C*, 2008, **112**, 1124-1131.

59. J. B. Joo, R. Dillon, I. Lee, Y. Yin, C. J. Bardeen and F. Zaera, *Proceedings of the National Academy of Sciences*, 2014, **111**, 7942-7947.